Copper and iron based thin film nanocomposites prepared by radio frequency sputtering. Part I: elaboration and characterization of metal/oxide thin film nanocomposites using controlled in situ reduction process

A. Barnabé · A. Chapelle · L. Presmanes ·
P. Tailhades

Abstract Copper and iron based thin films were prepared on glass substrate by radio-frequency sputtering technique from a delafossite $CuFeO_2$ target. After deposition, the structure and microstructure of the films were examined using grazing incidence X-ray diffraction, Raman spectroscopy, electron probe micro-analysis and transmission electron microscopy coupled with EDS mapping. Target to substrate distance and sputtering gas pressure were varied to obtain films having different amount and distribution of copper nanoparticles and different composition of oxide matrix. The overall reaction process, which starts from $CuFeO_2$ target and ends with the formation of films having different proportion of copper, copper oxide and iron oxide, was described by a combination of balanced chemical reactions. A direct relationship between the composition of the metal/oxide nanocomposite thin film and the sputtering parameters was established. This empirical relationship can further be used to control the composition of the metal/oxide nanocomposite thin films, i.e. the in situ reduction of copper ions in the target.

Introduction

Nanocomposites have been widely prepared and investigated due to their special properties which help in producing special engineering materials. In particular, nanometric metallic particles dispersed in an oxide matrix show special or improved physico-chemical properties [1–5].

A. Barnabé (✉) · A. Chapelle · L. Presmanes · P. Tailhades
Institut Carnot CIRIMAT—UMR CNRS 5085, Université Paul Sabatier Toulouse III, 118 Route de Narbonne, 31062 Toulouse Cedex 4, France
e-mail: barnabe@chimie.ups-tlse.fr

Nanocomposites composed of noble metals and metal oxides matrix are being considered as prospective materials for applications in catalysis, electronics, fuel cells and gas sensors [6–11]. It is known that instability of the size of noble metal clusters is one of the main reasons for the observed changes in reactivity of modified metal oxide surface. The fabrication processes and the phase stability of these metal and metal oxides were particularly studied [5, 12–14]. With thin films of these materials, there are different additional technological applications as in coated medical devices [15], magnetic recording media [16], electro-optical systems [17–19], photo-catalytic coatings [20, 21] or gas-sensing apparatus [10]. For the latter, it has been proven that the dispersion of small noble metal particles in an oxide matrix enhance or create optical sensitivity to different gases [22, 23]. Moreover, in the form of thin films, these materials allow mass production of devices at low cost with high control, repeatability and capabilities for miniaturization.

A lot of these applications require well-controlled film microstructures and, sometimes, precise spatial organization of metal particles in the oxide matrix. The deposition condition of the metal nanoparticles is a key parameter to control the properties of metal-oxide nanocomposite material. Several techniques have been used for the preparation of nanocomposite films. Among all the available processes, radio-frequency (RF) sputtering is the most suitable candidate for the preparation of materials with good homogeneity because it can operate under quite low oxygen partial pressures, over a wide range of temperatures and under various electronic, ionic and atomic bombings [24]. We have already shown that RF sputtering can lead to the preparation of copper based nanocomposite thin films with a control of the microstructure and self-assembly phenomena induced by post-annealing treatment when deposited on patterned substrates [25].

The aim of this paper is to provide evidence for controlled in situ reduction process of the mixed copper-iron oxide target by RF-sputtering method, in order to produce well characterized copper/oxide thin film nanocomposite.

Experimental methods

Preparation of $CuFeO_2$ sputtering target material

$CuFeO_2$ powder was prepared according to a well-established procedure by reacting stoichiometric mixture of commercial products Cu_2O and Fe_2O_3 [26]. This mixture was ground and heated in neutral atmosphere at 1000 °C for 24 h several times. X-ray diffraction of this product shows pure delafossite $CuFeO_2$ phase (Fig. 1). Delafossite has rhombohedral structure with the $R\overline{3}m$ space group. Lattice parameters determined by the Rietveld method are $a = 3.0344(2)$ Å and $c = 17.158(3)$ Å [27]. Sputtering target with 10 cm diameter was then prepared by pressing and heating $CuFeO_2$ powder at 950 °C for 12 h in nitrogen atmosphere. The as-prepared ceramic target was then adhered to a 12 cm diameter and 5 mm thick copper backing plate using silver paste to allow water cooling during the rf deposition process to prevent overheating.

Deposition of thin films

To produce desired thin films, the target assembly was attached to an Alcatel A450 RF sputtering chamber. The apparatus is equipped with a RF generator (13.56 MHz) device as well as a pumping system (a mechanical pump coupled with a turbo molecular pump). A pre-sputtering by argon plasma was performed for 10 min to clean the surface of the target from any impurities (water for instance)
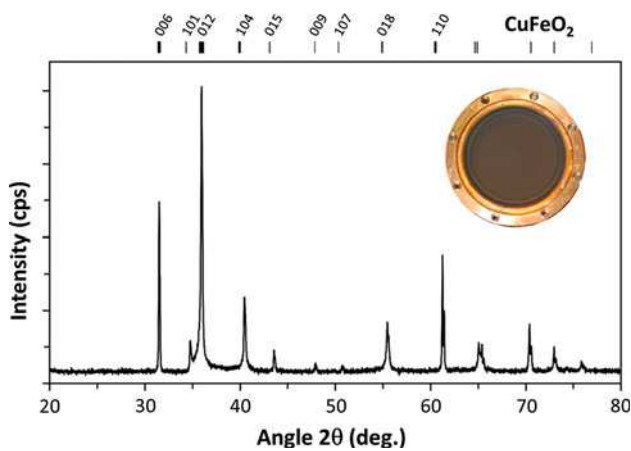
present prior to the film deposition. Pre-cleaned microscopic slides placed on a water cooled sample holder were used as conventional substrates. All films were produced with a RF power of 200 W by varying pressure and argon sputtering gas from 0.5 to 2.0 Pa, target to substrate distance (d) from 5 to 8 cm and deposition times. Four samples deposited with extreme pressures (0.5 and 2.0 Pa) and target-to-substrate distances (5 and 8 cm) are presented in this work and noted $P_{0.5}d_5$, $P_{0.5}d_8$, $P_{2.0}d_5$ and $P_{2.0}d_8$. For all samples, deposition rates (Table 1) were calculated from the deposition time and thickness of films determined using a Dektak 3030ST mechanical profilometer. Film thicknesses were set at 300 nm for all the characterizations except for transmission electron microscopy which required 50 nm thin films.

Thin film characterizations

The phase investigation of thin films was performed by grazing incidence X-ray diffraction (GIXRD) (grazing angle $\alpha = 1°$) using a Siemens D5000 diffractometer with the copper Kα radiation ($\lambda = 1.5418$ Å). Raman spectra were collected under ambient conditions using a fiber-coupled 532 nm laser and power of 1.1 mW with a Horiba Scientific Raman microscope fitted with a 100× objective lens. The final spectra is the average of three accumulations of 300 s. Examination of multiple spots showed that the samples were homogeneous. Chemical composition of the films was determined by electron probe micro-analysis (EPMA) using a Cameca SX 50 apparatus. Analyses were performed on films deposited on silicon substrate. The Si substrate provided an oxygen free support after the removal of the thin SiO_2 layer with hydrofluoric acid, from which the complete sample composition could be determined. The final average value corresponds to a minimum of ten measurements. Microstructural studies were carried out with a Veeco Dimension 3000 atomic force microscope (AFM) equipped with a super sharp TESP-SS Nanoworld© tip (nominal resonance frequency 320 kHz, nominal radius curvature 2 nm), and with a JEOL JSM 6400 field emission gun scanning electron microscope (FE-SEM). Diffraction, imaging and elemental analyses were made using a JEOL 2100F field emission gun transmission electron microscope (FE-TEM) operating at 200 kV and equipped with a X-ray energy dispersive spectroscopy (X-EDS) system. X-EDS chemical composition mapping were also performed in scanning TEM (STEM). TEM and STEM observations were carried out on films directly deposited on carbon covered nickel grids and cross-section specimens. For the latter, the thin film was cut into thin slices normal to the interfaces which were glued together between spacers and finally ion milled to perforation.

Fig. 1 XRD pattern of delafossite $CuFeO_2$ target and photography of the target assembly

Table 1 Process parameters for the deposition of metal oxide Cu/Cu$_x$Fe$_{3-x}$O$_4$ nanocomposites by rf-sputtering

Target material	CuFeO$_2$			
Substrates	Fused silica glass, Si-wafers, TEM grids			
Power (W/cm^2)	3.5			
Argon flow rate (sccm)	11–55			
Argon pressure P (Pa)	0.5–2.0			
Target to substrate distance d (cm)	5–8			
Deposition conditions	$P_{0.5}d_5$	$P_{0.5}d_8$	$P_{2.0}d_5$	$P_{2.0}d_8$
$P * d$ (Pa cm)	2.5	4.0	10	16
Deposition rates (nm/min)	6.77	3.11	10.1	3.75

Results and discussion

Structural analysis

Figure 2 shows GIXRD patterns of the as-deposited samples in the four deposition conditions. The intensity of characteristic (111) and (200) Bragg peaks of metallic copper are increasingly observed at $2\theta = 43.3°$ and $50.4°$ for the $P_{2.0}d_5$, $P_{0.5}d_8$ and $P_{0.5}d_5$ films. For all the four samples, no other dominant peak could be observed except a broad one located at $2\theta = 35.5°$, i.e. with $d_{hkl} \approx 2.5$ Å because of the nanocrystalline nature of films. It is difficult to match one particular phase to this peak, indeed it could be attributed to various nanocrystallized mixed oxide phases such as Cu$_2$O ($d_{111} = 2.46$ Å), CuO ($d_{111}= 2.52$ Å), CuFeO$_2$ ($d_{012} = 2.51$ Å), Cu$_x$Fe$_{3-x}$O$_4$ ($0 < x < 1$) ($d_{311} = 2.50$–2.52 Å).

Figure 3 presents Raman spectra of the as-deposited samples and the commercial references samples registered in the same experimental conditions. Signal from copper metal is not expected to appear in these spectra since it is Raman inactive in the range of measurement as Gong et al. demonstrated [28]. All the spectra exhibit Cu$_2$O characteristic bands located at 148, 218, 315, 405 and 622 cm^{-1}
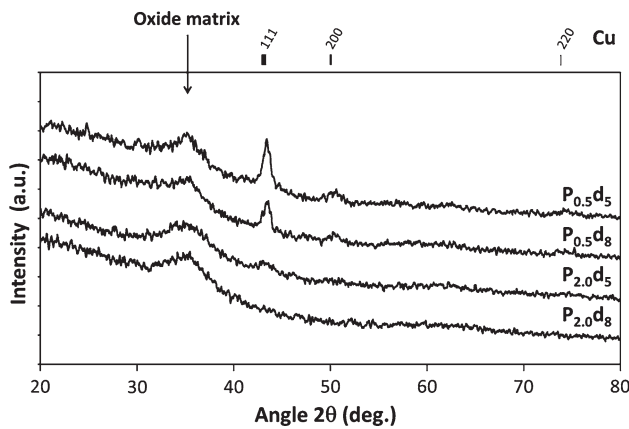
for the most intense ones [29–31]. Peaks located at 521 and 689 cm^{-1} can be assigned to Fe$_3$O$_4$ or Cu$_x$Fe$_{3-x}$O$_4$ with low copper content [32].

Heat treatments have been carried out in order to highlight the phases which could be crystallized or formed. Such treatments were carried out under primary vacuum to avoid oxidation. Figure 4 shows the GIXRD patterns of the annealed samples under vacuum at 450 °C for 12 h. The main peaks of copper metal are still visible in the samples deposited at $P_{0.5}d_5$, $P_{0.5}d_8$ and $P_{2.0}d_5$ indicating that these samples were not oxidized. In parallel, the characteristic peaks of delafossite CuFeO$_2$ phase appears for all the annealed films in association with a Cu$_x$Fe$_{3-x}$O$_4$ spinel phase for the $P_{0.5}d_5$ conditions. The Raman spectra of the annealed films (Fig. 5) are very different than those of the as-deposited samples. The bands of Cu$_2$O are no longer visible after annealing under vacuum. On the other hand, the two main characteristic bands of delafossite phase, located at 350 and 691 cm^{-1}, clearly appear. Moreover, a spinel phase close to Fe$_3$O$_4$, could be revealed by a signal observed at about 600 cm^{-1}, which becomes very low for

Fig. 2 GIXRD patterns of the $P_{0.5}d_5$, $P_{0.5}d_8$, $P_{2.0}d_5$ and $P_{2.0}d_8$ as-deposited samples
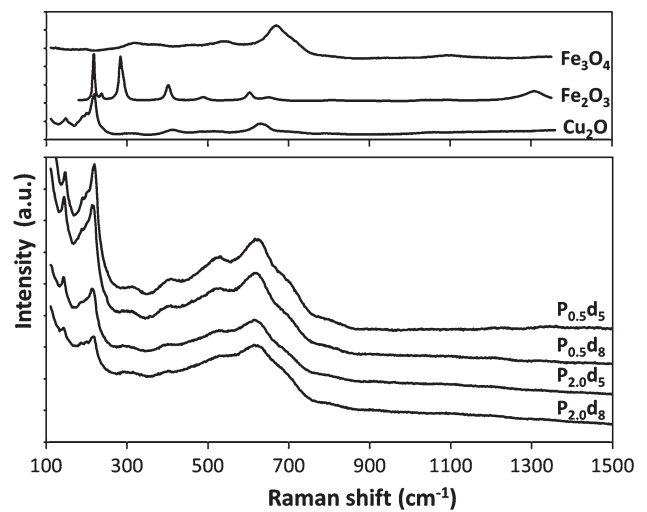

Fig. 3 Raman spectra of the $P_{0.5}d_5$, $P_{0.5}d_8$, $P_{2.0}d_5$ and $P_{2.0}d_8$ as-deposited samples. Raman spectra of commercial powders are also plotted for comparison
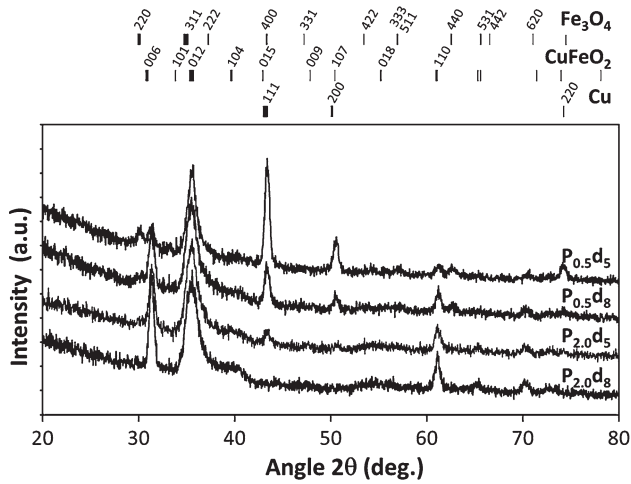
Fig. 4 GIXRD patterns of the $P_{0.5}d_5$, $P_{0.5}d_8$, $P_{2.0}d_5$ and $P_{2.0}d_8$ samples after post-annealing treatment at 450 °C for 12 h under primary vacuum
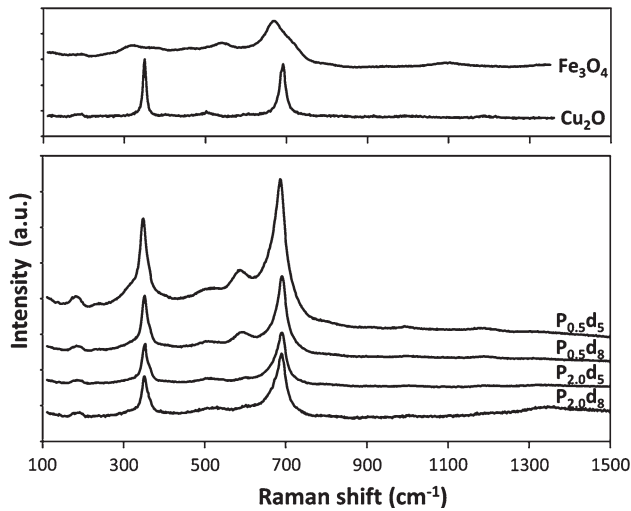

Fig. 5 Raman spectra of the $P_{0.5}d_5$, $P_{0.5}d_8$, $P_{2.0}d_5$ and $P_{2.0}d_8$ samples after post-annealing treatment at 450 °C for 12 h under primary vacuum. Raman spectra of commercial powders are also plotted for comparison

the samples prepared at low argon pressure. These observations are in agreement with the X-ray diffraction patterns, which clearly show the peaks of the delafossite phase and which also reveal some peaks of the spinel structure, mainly for the samples prepared at high argon pressure. However, the Raman band at about 600 cm^{-1}, does not match perfectly with that of pure magnetite powder. But the small shift toward the high wave numbers could be due to a small content of copper in the spinel phase [32].

Structural data given by both GIXRD and Raman spectroscopy allow us to describe the overall deposition process. For all the deposition conditions, Cu_2O and a $Cu_xFe_{3-x}O_4$ spinel phase are systematically present. In

addition, copper metal is detected for the films deposited at low $P * d$ product, as for instance, when the pressure of the argon sputtering gas is equal to $P = 0.5$ Pa. When annealed at 450 °C under primary vacuum, such films tend to form a delafossite phase associated with a spinel phase and metallic copper.

Copper metallic content

In the films deposited at $P_{0.5}d_5$, the cationic species coming from the target material, are partially reduced. Copper and ferrite are thus formed in place of delafossite, as predicted by the Cu–Fe–O phase diagram for lower oxygen partial pressure [33]. When the $P * d$ product increases, the amount of metallic copper decreases until it disappears for $P_{2.0}d_8$. As a result, the reduction process is adjustable with the sputtering parameters.

For the films deposited at low pressure, i.e. at $P = 0.5$ Pa, particles ejected from the target encountered a smaller number of collisions during the transfer from the target to the substrate. Accordingly, the mean free path of these particles is large and they are highly energetic. As a result, for the sample $P_{0.5}d_5$, particles arriving on the film tend to re-bombard the growing layer. The oxygen atoms are especially concerned by this re-bombardment due to their high sputtering yields (0.276 O/Ar) and low involved energies (5.83 eV/O) in comparison with iron (0.076 Fe/Ar, 9.91 eV/Fe) and copper (0.102 Cu/Ar with 10.71 eV/Cu) as simulated with the SRIM software [34, 35] for 80 eV incoming Ar$^+$ ions on delafossite $CuFeO_2$ material. The oxygen atoms could also form oxygen molecules into the gas phase that is pumped. The consequence of both this re-bombardment and oxygen loss due to the pumping system, is a growing layer with low oxygen content, i.e. with a more reduced state of the cationic species than the corresponding target material [36]. This behavior could be represented by the following reaction scheme:

$$CuFeO_2 \xrightarrow{\text{sputtering process}} Cu + \frac{1}{3}Fe_3O_4 + \frac{1}{3}O_2 \qquad (1)$$
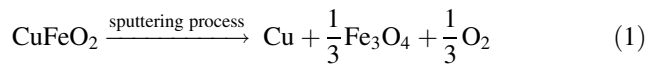
Composition of the oxide matrix

The formation of the delafossite phase when as-deposited films are annealed at 450 °C under primary vacuum, could be due to the reaction of Cu_2O, previously identified by Raman spectroscopy, with iron oxide, according to the following equation:

$$\frac{1}{2}Fe_2O_3 + \frac{1}{2}Cu_2O \rightarrow CuFeO_2 \qquad (2)$$
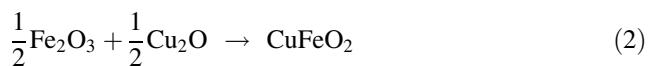
Such a reaction was already observed in previous work [37]. The hematite or α-Fe_2O_3 phase, was not observed in the as-deposited films (Fig. 3). However, the spinel oxide

revealed by the Raman spectroscopy could be due to the presence of the metastable γ-Fe_2O_3 or a mixed valence defect ferrite because both of which will display such a crystalline structure and could be observed due to the nanometric si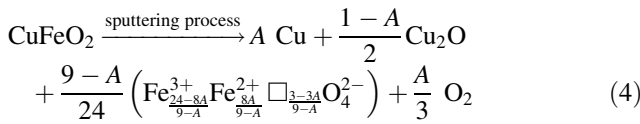ze of the crystallites in the films [38]. These metastable oxides could then react with the cuprite phase. Thus, the sputtering process could also form a spinel oxide and cuprite in the films, from the delafossite target, according to the following reaction scheme:
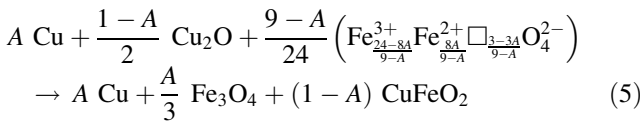
$$CuFeO_2 \xrightarrow{\text{sputtering process}} \frac{1}{2} \ Fe_2O_3 \ + \ \frac{1}{2} \ Cu_2O \tag{3}$$
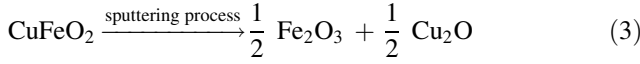
Overall deposition process

The overall deposition process, which starts from a $CuFeO_2$ target and ends with the formation of films made of different proportion of copper, copper oxide and iron oxide, could be schematically described by a balanced combination of Eqs. 1 and 3. This leads to the following global equation with $0 \leq A \leq 1$:

$$CuFeO_2 \xrightarrow{\text{sputtering process}} A \ Cu + \frac{1-A}{2} Cu_2O$$
$$+ \frac{9-A}{24} \left(Fe^{3+}_{\frac{24-8A}{9-A}} Fe^{2+}_{\frac{8A}{9-A}} \square_{\frac{3-3A}{9-A}} O^{2-}_4 \right) + \frac{A}{3} \ O_2 \tag{4}$$

The spinel oxide of Eq. 4, is a mixed valence defect ferrite which can be assumed as a combination of magnetite with γ-Fe_2O_3. The overall deposition process is then described by only one equation balanced with a ratio A, which is related to the reaction progress between the strict duplication of the target material $CuFeO_2$ and the complete reduction of the copper species. Equation 4 clearly points out the loss of oxygen ($A/3 \ O_2$) due to the sputtering process.

After a heat treatment at 450 °C under primary vacuum the delafossite phase is formed due to the reaction between the cuprite and the iron oxide according to Eq. 2:

$$A \ Cu + \frac{1-A}{2} \ Cu_2O + \frac{9-A}{24} \left(Fe^{3+}_{\frac{24-8A}{9-A}} Fe^{2+}_{\frac{8A}{9-A}} \square_{\frac{3-3A}{9-A}} O^{2-}_4 \right)$$
$$\rightarrow A \ Cu + \frac{A}{3} \ Fe_3O_4 + (1-A) \ CuFeO_2 \tag{5}$$

Even if phase identification allows us to qualitatively modelize the overall deposition process, the value of A cannot be fully estimated from the X-ray diffraction patterns analysis, because of poor crystallization of the oxide phases and their potential preferred crystalline orientation. Nevertheless, because of its cubic symmetry and the fact that the copper phase was already identified in the as-deposited samples, we can estimate that this metallic phase is not affected by preferred orientation and/or inhomogeneous crystallinity. As a result, a measurement of the integrated intensity of the copper (111) peak was done on GIXRD patterns for the as-deposited and annealed

samples (Table 2). The as-deposited and annealed samples do not exhibit the same integrated intensities due to the crystallization and instrumental accuracy, but a clear decrease in the relative amount of metallic copper for the films deposited at $P_{0.5}d_5$, $P_{0.5}d_8$ and $P_{2.0}d_5$ can be deduced and is presented in Table 2 with the average values normalized to the maximum. However, the real amount of copper metal, i.e. the real determination of the A ratio of Eq. 4 cannot be evaluated due to the unknown amount of the oxide phases.

Chemical analysis and quantitative phase determination

Electron probe micro-analysis measurements carried out on silicon substrates allowed us to determine the real iron, copper and oxygen content on as-deposited films. All the experimental data were fitted by iteration process on the base of single layer with a certain thickness, density, composition and oxidation state. The results of the iteration cycles were systematically validated by the calculated thickness which was always in perfect accordance with the thickness determined by a mechanical profilometer. The ratio between cations and oxygen for as-deposited samples and those annealed at 450 °C in vacuum are identical proving that the annealing treatment does not affect the oxygen content of the films. Results for annealed samples are reported in Table 3.

With the cation to oxygen ratio determined by EPMA, the oxygen loss ($A/3$ in Eq. 4) and thus the A ratio which corresponds to copper content can be calculated. This A ratio was found to be 0.31, 0.22, 0.12 and 0.03 for $P_{0.5}d_5$, $P_{0.5}d_8$, $P_{2.0}d_5$, and $P_{2.0}d_8$ respectively (Table 3). One can note that this EPMA analysis indicates that $A > 0$, i.e. there is a certain amount of metallic copper, in each sputtering condition within the limit of the accuracy of the technic. This is even true for the $P_{2.0}d_8$, whereas no metallic copper was previously detected by GXRD diffraction for both as-deposited and annealed samples.

Finally, the A ratio which gives the metallic copper content and the composition of the oxide matrix according to Eq. 4, is directly adjustable with the P and d experimental parameters and related to the inverse of the $P * d$ product. The relationship between A and $1/(P * d)$ for the four deposition conditions is shown in Table 3 and Fig. 6. It can be clearly observed that the copper content increases when the value of $1/(P * d)$ increases, i.e. when the particles lose less energy during the transfer from target to substrate.

Microstructural analysis

Various areas were systematically observed by TEM normal to the film plane, for each sputtering conditions. TEM micrographs of 50 nm thin films are presented in Fig. 7.

**Table 2** Relative amount of metallic copper determined by GXRD analysis

Deposition conditions $P * d$ (Pa.cm)	$P_{0.5}d_5$ 2.5	$P_{0.5}d_8$ 4.0	$P_{2.0}d_5$ 10	$P_{2.0}d_8$ 16
Copper (*111*) peak integration of the as-deposited samples (cps/sec/deg.)	20.5	12.7	4.4	–
Copper (*111*) peak integration of the vacuum annealed samples (cps/sec/deg.)	36.9	16.3	4.4	–
Relative average normalized copper content	100	50	15	0

Table 3 Chemical analysis determined by EPMA on annealed samples and quantification of the *A* ratio

Deposition conditions	$P_{0.5}d_5$	$P_{0.5}d_8$	$P_{2.0}d_5$	$P_{2.0}d_8$
$P * d$ (Pa cm)	2.5	4.0	10	16
$1/(P * d)$ (Pa^{-1} cm^{-1})	0.40	0.25	0.10	0.06
Cu	25.9(3)	25.8(3)	24.7(3)	25.3(3)
Fe	26.5(2)	26.0(2)	26.3(2)	25.0(2)
O	47.5(6)	48.2(6)	49.0(6)	49.6(6)
Cation to oxygen ratio	1.10(2)	1.07(2)	1.04(2)	1.01(2)
Calculated *A* ratio	0.31(3)	0.22(3)	0.12(3)	0.03(3)

All the TEM images show that the films consists of an homogeneous matrix and round shape particles. The homogeneous matrix is made of small grey particles of about 10 nm in diameter, which correspond to an oxide material with an average copper to iron ratio close to 0.5 as demonstrated by the representative TEM micrograph and EDS analysis shown in Fig. 8 for the $P_{2.0}d_5$ sample. This oxide matrix corresponds to the nanocrystallized oxide previously detected by GIXRD (Fig. 2). It was also evidenced by electron diffraction spots located at $d_{hkl} \approx 2.5$ and 1.3 Å represented in dashed lines in Fig. 8.

Within the oxide matrix we observe a distribution of round particles with much darker contrast for all the
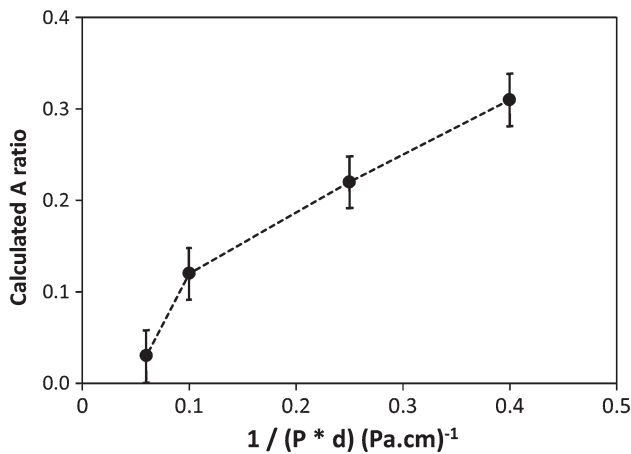
Fig. 6 Sputtering parameters (*P*, *d*) dependence of the copper metallic content and oxide matrix composition represented by the calculated *A* ratio

deposition conditions (Figs. 7, 8). In these particles, a very high concentration of copper is revealed by nano-EDS with a TEM probe of 2 nm. The characteristic diffraction rings of metallic copper, detected by ED and represented by continuous line in Fig. 8, clearly show that these round shape particles are metallic copper nanoparticles. The small amount of iron detected by EDS in these areas is due to superposition of the matrix and/or enlargement of the detected X-ray photons outside the copper particles. The average diameter of the round shape and black particles attributed to copper is close to 60–70 nm for the $P_{0.5}d_5$, $P_{0.5}d_8$ and $P_{2.0}d_5$ films and 40 nm for the $P_{2.0}d_8$ one. The particles sizes for the $P_{2.0}d_8$ sample are smaller than those measured for the other conditions, in accordance with the lower energy involved for this high pressure deposition condition [25]. The TEM analyzes revealed an homogeneous distribution of the copper particles in the samples and a decrease in copper metallic content with an increase of the $P * d$ product. Even for the high pressure and high distance deposition conditions ($P_{2.0}d_8$), metallic copper particles were detected in accordance with the EPMA measurements (Table 3). The small amount and small size of these copper particles associated with the grazing incidence configuration setup, explain that the characteristic diffraction peaks were not detectable in the GIXRD pattern for this sample (Fig. 4).

One can note that for a low substrate to target distance, rod-shaped particles were also visible in the whole analyzed area irrespective of the pressure used. A lower amount of these particles, which are moreover less dark probably due to a smaller thickness, was observed in the $P_{0.5}d_8$ films. The width of the rod-shaped particles is quite constant and is close to 10 nm. Isolated rod-shaped particles obtained in the $P_{0.5}d_8$ were analyzed in cross section view by TEM and STEM (Fig. 9). The film is made of a mixed oxide matrix with homogeneous distribution of copper, iron and oxygen as shown by the uniform distribution of Cu, Fe and O species. The slight variation of the contrast in the EDS mapping is only due to a progressive decrease of the thickness of the film from the substrate to the surface because of the thinning down process. The average particle size of the matrix is close to 10 nm and form a very dense array. A bigger particle is clearly visible in the upper part of the layer. No oxygen and iron content
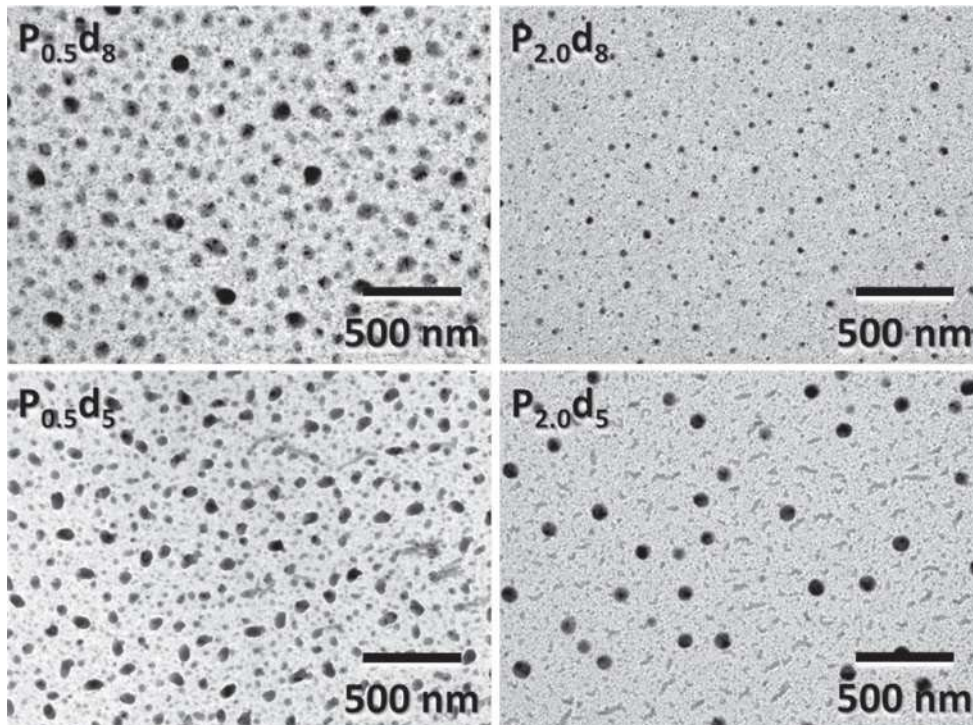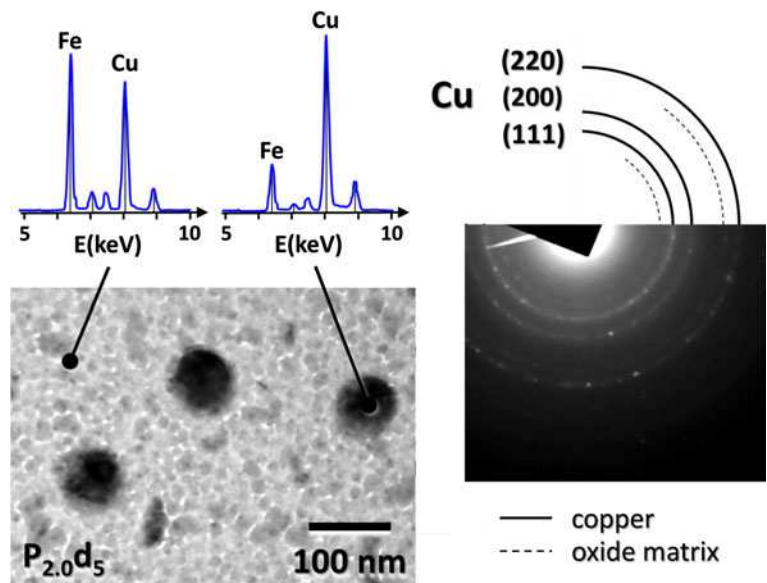
Fig. 7 TEM micrographs of the $P_{0.5}d_5$, $P_{0.5}d_8$, $P_{2.0}d_5$ and $P_{2.0}d_8$ as-deposited samples

Fig. 8 TEM micrograph and the corresponding ED pattern of the $P_{2.0}d_5$ as-deposited sample. Two representative X-EDS spectra are also indicated


are detectable in this area. This particle corresponds to the 60–70 nm round shape particle viewed on the normal TEM view (Fig. 7). In the lower part of the film, i.e. near the substrate interface, some long and thin particles are also visible. They are related to the rod-shape particles. The EDS mapping confirms that these particles are also made of pure copper. They have a similar dimension to the particle size of the matrix (10 nm) and form rods due to the high mobility of copper particles already evidenced by Mugnier et al. [39]. This mobility seems to be favored parallel to the substrate surface and generates such elongated particles only in the film plane. The growing of the copper particles in the perpendicular direction appears in the forms of bigger round-shape particles.

Summary and conclusion

The effects of pressure of the argon sputtering gas ($0.5 \leq P \leq 2.0$ Pa) and target to substrate distance

Fig. 9 Cross section TEM micrograph and EDS mapping obtained at oxygen, copper and iron Kα edges in STEM mode for the $P_{0.5}d_8$ as-deposited sample
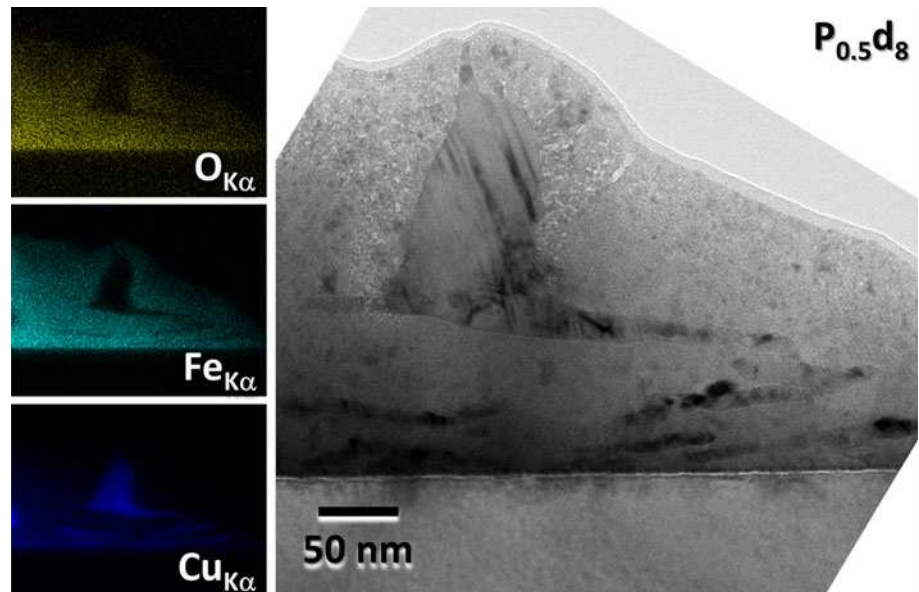
(5 ≤ d ≤ 8 cm) upon the structure and the microstructure of Cu–Fe–O films have been investigated for RF sputtering of a homemade CuFeO$_2$ target. The formation of copper nanoparticles within a mixed oxide matrix has been systematically observed in this process window. A correlation between P and d in one hand and the structural and chemical composition of the phases on the other hand, have been established. The metallic copper content of the films deposited at low $P * d$ product (i.e. $P_{0.5}d_5$) is almost eight times higher than that of the films deposited at the highest $P * d$ product. This decrease in the metallic copper content is associated to a change in the oxide matrix. The overall deposition process has been described by one equation balanced by a ratio A. This ratio is directly adjustable with the P and d experimental parameters represented by the $P * d$ product. The morphology and the distribution of the copper particles have also been characterized on normal and cross-section views, by electron microscopy analyses. As a result, copper/oxide thin film nanocomposites have been prepared and characterized in this work, using controlled in situ reduction process. The control of the in situ reduction process yielded in different quantity, size and shape of copper nanoparticles in association with a matrix of several oxides.

References

1. Sekino T, Niihara K (1997) J Mater Sci 32:3943. doi: 10.1023/A:1018668900343
2. Gugilla S, Manthiram A (1996) Mater Sci Eng B 40:191
3. Chakravorty D (1992) Bull Mater Sci 15:411
4. Moya JS, Lopez-Esteban S, Pecharroman C (2007) Prog Mater Sci 52:1017
5. Kondo H, Sekino T, Tanaka N, Nakayama T, Kusunose T, Niihara K (2005) J Am Ceram Soc 88:1468
6. Yashima M, Falk LKL, Palmqvist AEC, Holmberg K (2003) J Colloid Interf Sci 268:348
7. Seino S, Kinoshita T, Otome Y, Maki T, Nakagawa T, Okitsu K, Mizukoshi Y, Nakayama T, Sekino T, Niihara K, Yamamoto TA (2004) Scripta Mater 51:467
8. Moreau F, Bond GC, Taylor AO (2005) J Catal 231:105
9. Basu S, Basu PK (2009) J Sens ID 861968:1
10. Korotcenkov G, Cho BK, Gulina L, Tolstoy V (2009) Sens Actuators B 141:610
11. Singh N, Gupta RK, Lee PS (2011) Appl Mater Interfaces 3:2246
12. Hwang HJ, Toriyama M, Sekino T, Niihara K (1998) J Eur Ceram Soc 18:2193
13. Yoona S, Dornseiffer J, Xiong Y, Grünerc D, Shen Z, Iwaya S, Pithan C, Waser R (2011) J Eur Ceram Soc 31:773
14. Sasaki T, Koshizaki N, Koinuma M, Matsumoto Y (1999) Nanostruct Mater 12:511
15. Randeniyaa LK, Bendavid A, Martin PJ, Amin MS, Rohanizadeh R, Tang F, Cairney JM (2010) Diamond Relat Mater 19:329
16. Wang H, Xue SX, Yang FJ, Wang HB, Cao X, Wang JA, Gao Y, Huang ZB, Yang CP, Cheung WY, Wong SP, Li Q, Li ZY (2006) Thin Solid Films 505:77
17. Tseng CC, Hsieh JH, Wu W (2011) Thin Solid Films 519:5169
18. Vasquez-Cuchillo O, Pal U, Vasquez-Lopez C (2001) Sol Energy Mater Sol Cells 70:369
19. Winkler T, Schmidt H, Flügge H, Nikolayzik F, Baumann I, Schmale S, Weimann T, Hinze P, Johannes HH, Rabe T, Hamwi S, Riedl T, Kowalsky W (2011) Org Electron 12:1612
20. Yu J, Xiong J, Cheng B, Liu S (2005) Appl Catal B 60:211
21. Hsieh JH, Shang CC, Chang YK, Cherng JS (2010) Thin Solid Films 518:7263
22. Ando M, Kobayashi T, Haruta M (1994) J Chem Soc 90:1011
23. Ando M, Chabicovsky R, Haruta M (2001) Sens Actuators B 76:13
24. Mauvernay B, Presmanes L, Capdeville S, De Resende VG, De Grave E, Bonningue C, Tailhades P (2007) Thin Solid Films 515:6532
25. Mugnier E, Barnabé A, Presmanes L, Tailhades P (2008) Thin Solid Films 516:1453
26. Mugnier E, Barnabé A, Tailhades P (2006) Solid State Ion 177:607
27. Lalanne M, Barnabé A, Mathieu F, Tailhades P (2009) Inorg Chem 48:6065

28. Gong YS, Lee C, Yang CK (1995) J Appl Phys 77:5422
29. Fu Q, Jin P, Ling X, Zhang S, Sun W, Xia Y (2012) Int J Corr 2012:1
30. Zheng YT, Xuan FZ, Wang Z (2012) Mater Lett 78:11
31. Colomban P, Tournié A, Maucuer M, Meynard P (2012) J Raman Spectrosc 43:799
32. Varshney D, Yogi A (2010) Mater Chem Phys 123:434
33. Katkov AE, Lykasov AA (2003) Inorg Mater 39:171
34. Ziegler JF (2008) SRIM software—the stopping and range of ions in matter. http://www.srim.org/
35. Ziegler JF, Biersack J, Littmark U (1985) Pergamon Press The Stopping and Range of Ions in Matter
36. Ben Amor S, Rogier B, Baud G, Jacquet M, Nardin M (1998) Mater Sci Eng B 57:28–39
37. Barnabé A, Mugnier E, Presmanes L, Tailhades P (2006) Mater Lett 60:3468
38. Tailhades P, Gillot B, Rousset A (1997) J Phys IV C1:249
39. Mugnier E, Pasquet I, Barnabé A, Presmanes L, Bonningue C, Tailhades P (2005) Thin Solid Film 493:49